Gas–liquid two-phase bubble flow spinning for hydrovoltaic flexible electronics

Yuanming Cao[1], Ji Tan[2], Tingting Sun[1], Yechuan Deng[2], Min Zhang[1], Shiwei Guan[2], Xianming Zhang[2], Chao Wei[2], Panpan Huo[1], Mingpeng Zhuo ®[3], Hongqin Zhu[2], Jiajun Qiu ®[2] ✉ & Xuanyong Liu ®[1,2] ✉

Hydrovoltaic technologies that generate electricity by absorbing or transferring free water without chemical reactions have been explored as potential candidates for renewable energy. Self-powered flexible sensors, including hydrovoltaic fibers, are becoming an important research direction in the field of renewable energy. However, integrating sensing and power generation in functional fibers remains challenging due to the need to regulate water movement to achieve performance differences. Here, we present a gas-liquid two-phase flow spinning method, inspired by spider multimodal spinning, that uses bubble-triggered spinning-liquid deformation to fabricate hollow, solid spindle, and ratchet tooth-shaped fibers. These structures alter water adsorption and transfer behaviors, making them suitable for targeted applications in hydrovoltaic devices for energy and sensing fields. Shaped fibers prepared from alginate-bridged MoS_2 enable a wide range of hydrovoltaic applications. The obtained fiber has a power density of 2.18 mW/cm³, stable operation at 2.1 V for 43 hours, and sensitivity of 9.36 mV/RH%/s, leading to the development of smart masks for nasal cycle monitoring, diagnosis, and therapy as potential applications. Spinning materials were extended to materials such as carboxymethyl cellulose, polyvinyl alcohol, etc., inspiring the design of structure-responsive hydroelectric materials and advancing textile electronics.

Harvesting energy from human and environmental interactions with water interfaces, without chemical reactions[1–3], has been applied to promising areas like self-powered wearables and the Internet of Things (IoT)[4–9]. Various flexible materials based on carbon blacks[10,11], metal oxides[12,13], and transition metal dichalcogenide (TMDC)[14,15] are prepared that have been generally developed in wearable energy supply[16], respiration sensing[17], and sweat monitoring under the guidance of the aforementioned hydrovoltaic effect. One-dimensional (1D) fibers are flexible, lightweight, and ideal for wearable energy harvesting and self-powered flexible sensors applications[18]. Fiber surfaces are customized with individual geometries, such as cycloidal structures for directional water transport[19] and spindle structures for enhanced surface energy[20]. A controlled water management capability is essential for hydrovoltaic energy output[4]. However, challenges in controlling their structure and properties highlight the need for advanced fabrication methods. The versatile spider silk spun by spiders provides inspiration for fiber fabrication for multi-scenario application as well as the various biological microstructures exhibiting controllable water droplet condensation and transport properties inspire the modulation of the hydrovoltaic effect[21,22] (Supplementary Text S1). Intriguing water-

[1]State Key Laboratory for Modification of Chemical Fibers and Polymer Materials, College of Biological Science and Medical Engineering, Donghua University, Shanghai, China. [2]State Key Laboratory of Advanced Ceramics, Shanghai Institute of Ceramics, Chinese Academy of Sciences, Shanghai, China. [3]Institute of Functional Nano and Soft Materials (FUNSOM), Jiangsu Key Laboratory for Carbon Based Functional Materials and Devices, Soochow University, Suzhou, China. ✉e-mail: qiujiajun@mail.sic.ac.cn; xuanyong@dhu.edu.cn

harvesting examples include cacti transport harvested fog from their spine tips to their roots[23]; spider silk transports captured fog or dew from periodic spindle knots to joints[24]; and *Nepenthes alata* delivers liquids or nectar directionally from the inner to outer edge of its peristome using multiscale structures[25]. These outstanding structures facilitate efficient water collection and transport, providing a favorable foundation for hydrovoltaic power generation[26,27]. The movement of water on the material surface aligns with the moving boundary of the electrical double layer (EDL) model, expressed as $V = kv \propto \frac{dL}{dt}$[28,29], where L is the contact length of the moving boundary, k is the material coefficient, and v is the water transfer velocity. Such insights have guided our design of tunable fiber structures, dimensions, and material parameters, opening up endless possibilities for advancements in the hydrovoltaic field.

A simple and controllable technology to build a variety of structural fibers with excellent performance needs to focus on breakthrough development. Various artificial bioinspired fibers have been developed, such as spider silk with spindle knots[30], helical cracking spindle fibers[31], and necklace-structured fibers[32]. Periodic fiber knots have been fabricated via Rayleigh instability-driven methods such as dip-coating[20,33] and electrostatic forces[34]. Notably, hemline-shaped microfibers formed by tuning jet dynamics under piezoelectric vibrations provide a novel approach for open-fluid transport[35]. These resulting spindle-knot microfibers exhibit interesting interactions with water. However, the application of these methods is largely limited by insufficient control over fluid and fiber morphology[36]. Recently, wet-spinning (microfluidic spinning) techniques have been successfully used to generate spherical structures on microfibers by introducing oil or gas phases, thereby producing spindle-knot microfibers[37,38]. These knotted fibers possess additional functionalities, such as droplet encoding[39], cell-encapsulation[32], and superhydrophobic/super-omniphobic surface[40]. Notwithstanding these advances, there are still several key issues that inhibit the wider application of biomimetic fibers: firstly, the shaped fiber currently reported are limited to the spindle or spherical shapes; secondly, although perfusable hollow channels offer a wide choice of spherical model viability, they remain difficult to achieve multimodal biomimetics; thirdly, the geometrical

structure induces water transfer on electronic effects, especially applied in the wearable field.

Early in the 18th century, *James Watt* (1736–1819) improved the steam engine condenser, leading scientists to gradually study the behavior of steam-water mixtures. This mixed gas–liquid flow phenomenon is now known as two-phase flow (Fig. 1A), which is widely applied in mass transfer and heat dissipation fields such as oil and gas transport pipelines, heat transfer in nuclear reactor cooling systems, and the migration of groundwater and pollutants[41]. The precise regulation of bubble dynamics via customized microfluidic platforms expands the frontiers of multiphase interfacial material fabrication, offering scientific insights into programmable interfacial engineering[42]. In this paper, we report a gas–liquid two-phase flow spinning method, whose mechanism is derived from the bubble flow pattern generated by the gas phase in the liquid phase. The bubble-triggered gel structure transforms into shaped fibers with defined shapes when the spinning liquid enters the critical point between the tip of the needle and the solidification bath. This method has been utilized to produce over four types of functional soft fibers with different surface morphologies without the need to change or modify the spinneret holes. The 2D TMDCs represented by MoS_2 are the best candidates for this strategy, and due to the special energy band structure, semiconductors, and excellent mechanical properties[43], they have been proven to be promising materials for hydropower generation due to water-induced proton diffusion[44]. Our gas–liquid two-phase flow spinning technology overcomes the drawbacks of single fiber surface morphology, which are commonly used in traditional spinning methods (Supplementary Text S2, Table S1 and Fig. S1). This method is less costly and has a simpler process than other spinning methods.

The resulting cavity spindle fibers exhibit a water uptake of 414%, solid spindle fibers achieve a fog collection capacity of 44.6 μL/mm, and concavity ratchet fibers demonstrate a water transfer speed of 6890 μm/s. Uniquely, we designed a sodium alginate (SA)-bridged 1T-MoS_2 hydrovoltaic spinning drop and integrated it with these fiber structures, achieving excellent electrical properties, including a power density of 2.18 mW/cm³, stable operation for 43 hours at 2.1 V, and high
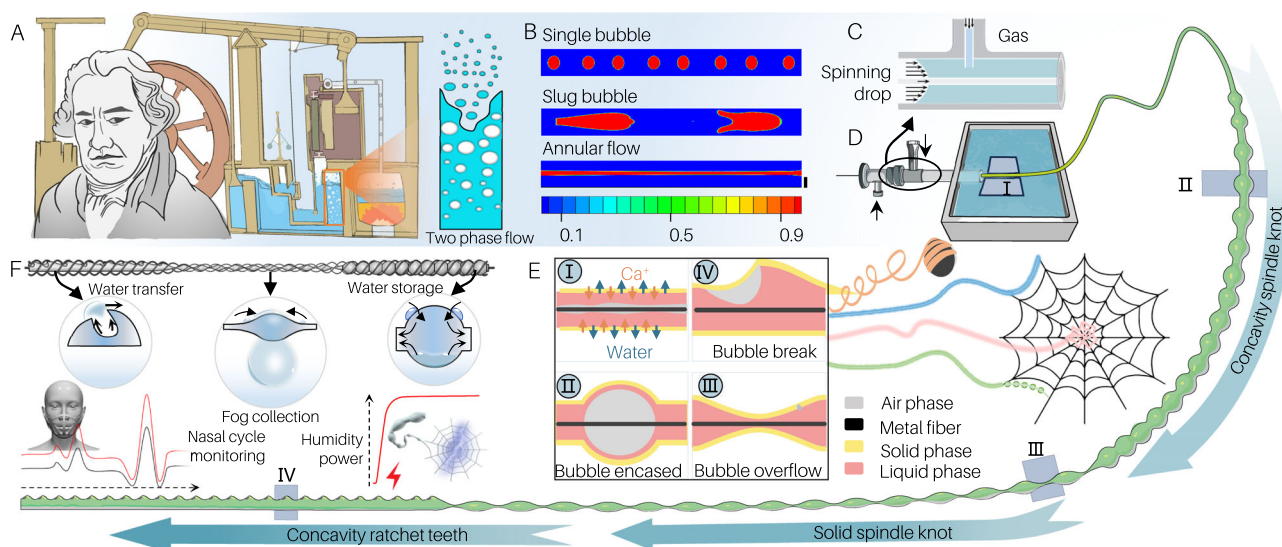
Fig. 1 | Illustration of bioinspired spinning approach for producing multi-morphological functional fibers. A A diagram of a steam engine condenser illustrates the behavior of the steam-water mixture within. This gas–liquid mixture flow phenomenon is now termed two-phase flow. **B** Single bubble, slug bubble, and annular flow simulated by computational fluid dynamics for two-phase flow pattern with the gas superficial velocity (j_g), water superficial velocity (j_l) in a horizontal pipe. **C**, **D** Continuous preparation of multi-morphic fibers by gas–liquid two-phase flow-assisted wet spinning. Schematic cross-section of bioinspired multi-morphic fibers including E_I traditional cylindrical, E_{II} cavity spindle knot, E_{III} solid spindle knot, and E_{IV} concavity ratchet teeth. **F** A schematic diagram of the water storage and power generation applications of a cavity spindle knot structure, the fog collection application of a solid spindle, and the concave ratchet structure for rapid water transportation and sensing applications. Scale bar: 1 mm.
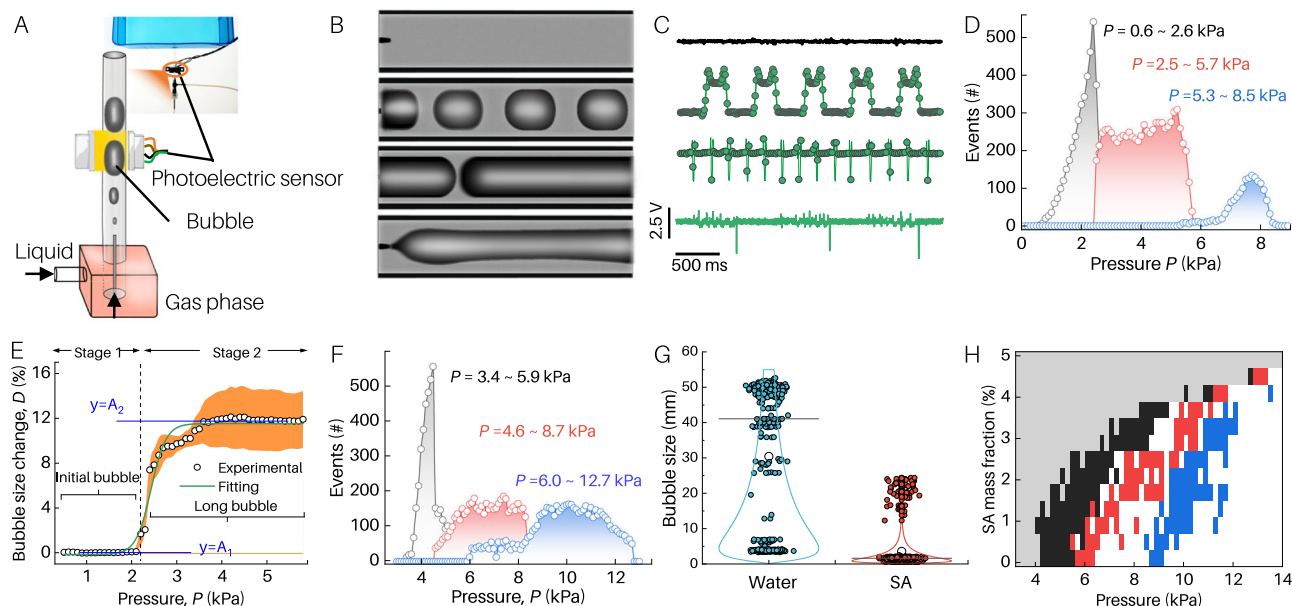
Fig. 2 | Fluid properties of the water and SA. A Schematic of the bubble flow pattern characterization setup. **B** The pictures of the bubble flow pattern, and **C** the corresponding electrical signals of the control, single bubble, slug bubble, and annular jet (air pressure 0, 0.8, 3.8, and 7.2 kPa from top to bottom, the water flow rate is 0.03 cm³/s). **D** Graphs of bubble flow patterns with three representative regions are estimated at 0.6–2.6, 2.5–5.7, and 5.3–8.5 kPa. **E** Bubble size changes (normalized to the initial bubble length value) as a function of pressure. **F** The representative bubble flow pattern of SA has a pressure range of 3.4–5.9, 4.6–8.7,

and 6.0–12.7 kPa, the corresponding gas flow rates (Q_g) of 3.68–4.85, 4.25–5.86, 4.87–7.08 cm³/s and SA flow rate (Q_l) of 0.05 cm³/s, the concentration (C) of SA was 25 mg/mL. **G** Box plot (each dot represents one test) of bubble size at the two corresponding regions of bubble flow pattern, estimated to be 30.4 ± 21.3, 3.5 ± 6.0 (values are reported as mean ± standard deviation, $n = 520$ independent tests for water, $n = 540$ for SA, black circle: mean, horizontal line: median). **H** Phase diagram of bubble formation under different pressures and SA (Sodium alginate) mass fraction (The SA flow rate is 0.05 cm³/s).

sensitivity of 9.36 mV/RH%/s. Finally, the bubble-triggered gel structure transition mechanisms and hydrovoltaic generation principles were revealed through numerical simulations and model analysis. We illustrate the potential of fibers in textile electronics by extending the gas–liquid two-phase flow spinning method to prepare polymorphic functional fibers based on polyvinyl alcohol and sodium hydroxyethyl cellulose.

Results

Bionic concepts, principles, and applications of gas–liquid two-phase flow for spinning multi-structured fibers

The flow patterns of gas–liquid two-phase flow were simulated and analyzed in a horizontal pipeline. The gas–liquid two-phase flow adaptively forms single bubble, slug bubble, and annular flows (Blue: liquid phase, red: gas phase) (Fig. 1B, see Supplementary Text S3 and Fig. S2). Each regime exhibited distinct volume fraction differences (Supplementary Fig. S3). The velocity profiles revealed vertical shear slip decreases to zero while horizontal shear slip increases and concentrates (Supplementary Fig. S4A–C), indicating negligible transverse mass flow compared to longitudinal flow. Given the temporal stability of bubble shapes post-formation, flow regimes were classified based on liquid (J_l) and gas (J_g) superficial velocities (Supplementary Fig. S4D). Porosity (ε) and pressure drop (ΔP) showed <20% deviation from mass conservation laws for incompressible flow (Supplementary Fig. S4E, F). A spider spinneret-inspired nozzle (Fig. 1C, D, Supplementary Fig. S5), designed using gas–liquid flow dynamics, was fabricated via gas-assisted wet-spinning. Fiber structures were rapidly stabilized by Ca^{2+}-induced crosslinking upon gas–liquid contact (Fig. 1E_I). Low-energy single bubbles formed hollow spindles via drop encapsulation (Fig. 1E_II), while slug flows generated solid spindles upon rupture (Fig. 1E_III). Annular jets produced ratchet-like structures under high shear (Fig. 1E_IV). The above cross-sections are shown in Supplementary Fig. S6A. A SA/1T-MoS₂ spinning solution was developed through sequential bridging (Supplementary Fig. S6B). Convincingly, in the further preparation of electronic fiber (e-fiber), cavity spindle

knot fibers exhibited enhanced power generation via optimized water retention (Fig. 1F right). Solid spindle fibers achieved efficient mist collection (Fig. 1F middle). Ratchet fibers enabled respiratory sensing through directional water transport (Fig. 1F left).

Fluid properties of gas–liquid two-phase flow

The multiphase flow characteristics were first verified via a photoelectric sensor (PES)-based gas–liquid mixing pipeline (Fig. 2A, B and Supplementary Fig. S7A). In contrast to the flat signal from the control without airflow (top of Fig. 2C), the photoelectric signal was detected by the length and diameter of the generated bubbles (Supplementary Fig. S7B). There were three different response waveforms, and bubble length (D) statistically averaged at 3.77, 34.38, and 100 mm, respectively (Fig. 2B and Supplementary Fig. S7C–E). The pressure distributions were 0.6 to 2.6 kPa with 3.63 mm for a single short bubble, 2.5–5.7 kPa with 34.5 mm for slug bubble, and 5.3–8.5 kPa for annular flow, respectively (Fig. 2D). These experimental findings showed strong agreement with numerical simulations, confirming that bubble volume changes during gas–liquid mixing arise from incompressible fluid pressure effects. However, the typical enlargement of bubbles in water pipes did not appear in the experiment due to the dynamic phase interface interactions (Supplementary Fig. S8A), rather the length of the slug bubble increases with pipe growth (Supplementary Fig. S8B). A profile of the bubble size (length) changes is presented by video analysis (Fig. 2E). At initial pressures (0.6–2.1 kPa, single bubble regime), bubble length remained stable ($\Delta D < 0.1\%$), while beyond 2.1 kPa, axial elongation dominated until 5 kPa, transitioning to exponential radial expansion (ΔD up to 15%) during nozzle detachment (slug-bubble regime). This nonlinear phase evolution is captured by the empirical model (Supplementary Text S4):

$$D = A_2 + \frac{A_1 - A_2}{1 + e^{(p-p_0)/dp}} \tag{1}$$

Where $D\%$ is the percentage change in diameter, A_1 is the average length of the short bubble, A_2 is the average diameter of the slug bubble, and p is the pressure change in the pipe. The experimental data (unfilled black dots) conformed well with the fitting results (green curve, $R^2 = 0.98$). Such broad distributions of bubbles can be attributed to the use of non-Newtonian fluids like SA, which promote the formation of stable, controllable, and dynamic two-phase flow structures, thereby establishing optimal material preparation conditions (Fig. 2F). The pressure ranges in the SA solution were 3.4–5.9 kPa for single bubbles, 4.6–8.7 kPa for slug bubbles, and 6.0–12.7 kPa for annular flow. Higher viscosity shortens bubble expansion and pinch-off, reducing size. Additionally, viscosity-mediated pulling forms elongated necks that shear off into bubbles during spinning. Higher SA viscosity generates smaller bubbles under constant gas pressure (Supplementary Fig. S8C, D). Increasing liquid flow enhances viscous shear, shortening slug bubbles (Supplementary Fig. S8E), while Newtonian fluids show the opposite trend. Higher gas flow aids yield stress fluid breakthrough, increasing slug bubble length and formation rate. For jet formation, shear stress rises with shear rate, while viscosity drops due to weakened molecular interactions (Supplementary Fig. S8F), promoting annular flow jet transition. The spinning process allows precise control of microbubble spacing ($\lambda = 0$ - 5 mm) and diameter ($d = 0.3$ - 2.5 mm) by modulating gas pressure (0.02 - 0.1 kPa s^{-1}) (Supplementary Fig. S9A–D). Viscoelastic encapsulation avoids bubble fusion during deformation through reinforced interfacial films (Supplementary Fig. S9E), contrasting with Newtonian fluids that fuse instantly upon contact (Supplementary Fig. S9F). Bubble fusion occurs cyclically after $n = 6 \pm 1$ bubbles, marked by distinct waveform signatures (Supplementary Fig. S9G, H). Compared to water, bubble size polarization is more pronounced, with distinct transitions from single bubbles to slug flow (Fig. 2G, Supplementary Text S4). Hydrophilic channels ($\theta = 35°$) generate 30% longer bubbles at lower frequencies (13 Hz vs. 17 Hz) due to precursor film propagation, reduced shear, and capillary-dominated breakup. Wettability governs liquid film stability in annular flow and elongates bubbles through compression-driven pinch-off in slug flow (Supplementary Fig. S10). Photoelectric signal curves demonstrate that the SA liquid phase has a more uniform distribution, indicating improved bubble stability and controllability (Supplementary Fig. S11). By modulating gas-phase pressure, the flow rate of the SA spinning drop was precisely controlled to obtain various flow patterns (Fig. 2H).
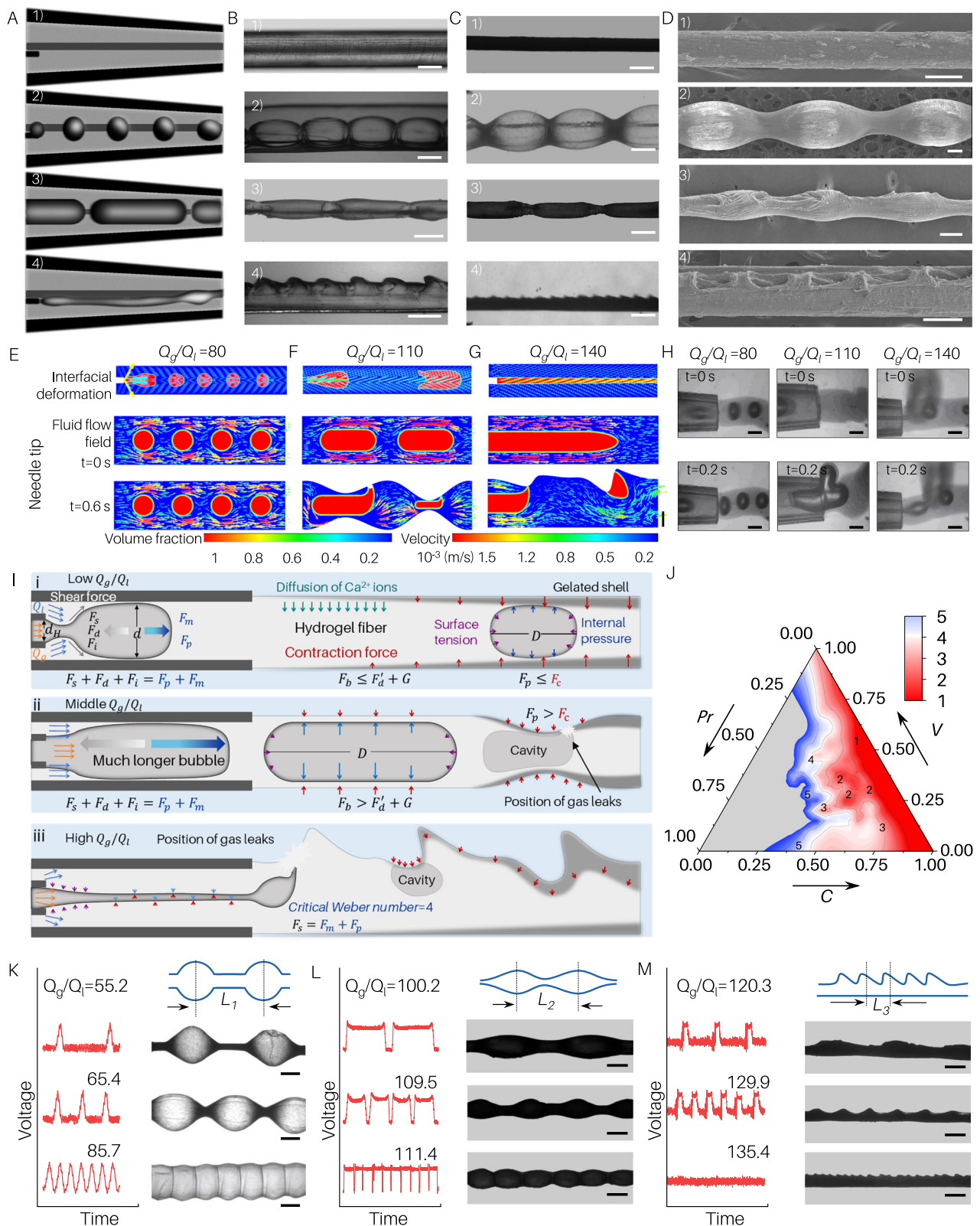
The gas–liquid two-phase flow for fibers fabrication and mechanism

A gas-assisted wet-spinning system that mimics the versatile spinning of spiders is designed (Supplementary Fig. S12). Specifically, at zero gas-to-liquid ratio (Q_g/Q_l), conventional cylindrical fibers formed (Fig. 3A$_1$–D$_1$). Increasing Q_g/Q_l to 88 induced hydrated microfibers with hollow joints, termed cavity spindle knot (CSK) fibers (Fig. 3A$_2$–D$_2$; Supplementary Fig. S13A–C). Further escalation to $Q_g/Q_l = 107$ triggered slug bubble formation, producing segmented gel fibers that dried into solid spindle knot (SSK) fibers (Fig. 3A$_3$–D$_3$). At $Q_g/Q_l = 136.6$, annular jet flow generated fibers with concave ratchet teeth (CRT) structures (Fig. 3A$_4$–D$_4$; Supplementary Fig. S13D–F). Excessive airflow caused coarse annular flow, yielding mixed spindle morphologies (Supplementary Fig. S14). The fluid dynamics of as-spun fibers were investigated through computational simulations of two-phase flow states (Fig. 3E–G and Supplementary Fig. S15). Upon gas introduction, velocity equilibration occurs at the gas–liquid interface, governed by the flow rate ratio Q_g/Q_l and viscosity ratio μ_g/μ_l. Low gas–liquid flow ratios (Q_g/Q_l, $V_g < V_l$) induce viscous drag-driven elongation of Taylor bubbles, culminating in capillary pinch-off to produce monodisperse bubbles with diameters scaling as the cubic root of the viscosity-to-surface-tension ratio (Fig. 3E, Supplementary Fig. S15A, G). Post-detachment, interfacial tension preserves spherical morphologies,

consistent with microfluidic studies (Fig. 3H left panel and Supplementary Figs. S15B and S16A). At intermediate Q_g/Q_l ($V_g \approx V_l$), bubble evolution follows three stages (Fig. 3F and Supplementary Fig. S15C): initial radial expansion balances shear stress, defining maximum neck width; radial compression and axial stretching drive strain-hardening and gradual elastic energy release; and post-pinch-off, shear tapering and capillary waves shape interfacial features. Slug flow dominance initiates pressure-gradient-driven cavity collapse, where viscoelastic stress relaxation pathways direct energy redistribution into spindle-shaped neck morphologies (Fig. 3H middle panel and Supplementary Figs. S15D and S16B). At high Q_g/Q_l ($V_g \gg V_l$), the elongated Taylor bubbles coalesce into continuous gas cores, and annular jet can be accelerated by shear force (Fig. 3G, Supplementary Fig. S15E, H). Viscous entrainment thins the liquid core, stabilizing Taylor cone structures. Upon ejection, the jet penetrates the gel matrix, dissipating kinetic energy (Supplementary Fig. S15F, I). Rayleigh–Plateau instability and interfacial shear induce flow instability, forming ratchet-like surface patterns (Fig. 3H right panel and Supplementary Fig. S16C).

The mechanisms of the gas–liquid two-phase flow spinning method was inferred (Fig. 3I). Extruded SA instantaneously formed an outer gel layer that thickened inward via Ca^{2+} diffusion, generating contraction force (F_c). Concurrently, hydrogel fibers moved horizontally in CaCl$_2$ solution, guided by the pulling action of the core wire (Supplementary Fig. S17A, B). Airflow introduction triggered bubble detachment at transitional regions governed by force equilibria on bubble length D (Supplementary Fig. S17C), expressed as: $F_s + F_d + F_i = F_p + F_m$, where F_s, F_d, F_i, F_p, and F_m represent surface tension, viscous drag, inertia, pressure force and gas momentum force. The bubble-triggered spinning-liquid deformation mechanism determines bubble length through dynamic competition between interfacial forces: surface tension stabilizes bubble interfaces, while viscous shear promotes elongation, and modulated by momentum-driven inertial effects. The equilibrium length, given by D = $L_c[S^* + L^* + T^*]^{1/4}$·, scales nonlinearly with contributions from capillary, viscous, and inertial dynamics, where S^* (surface-tension dominance), L^* (viscous shear effects), T^* (momentum transfer) and L_c represent the capillary length scale. The length D determines the buoyancy force (F_b) and resistance ($F'_d + G$, where F'_d is downward viscous drag force, G is gravity of a bubble) in the vertical direction. The bubbles flowing out of the needle tip will be subjected to the internal pressure (F_p) of the bubbles and the contraction force (F_c) of the dehydration of the gel (Supplementary Fig. S17D). At a low Q_g/Q_l ratios, $F_b \le F'_d + G$ and $F_p \le F_c$, a single bubble can stably exist. The D increases as Q_g/Q_l reaches the medium range, $F_b > F_d + G$ and $F_P > F_c$, bubbles leak at weaker points and contract into spindles. The annular jet state is high Q_g/Q_l ratio, a jet forms only if (i) the force generated by gas momentum exceeds surface tension and (ii) surface tension cannot form spherical or near-spherical bubbles. This occurs at a critical Weber number of 4, simplifying the force balance to $F_p + F_m = F_s$. The gas velocity accelerates under shear forces[45], but as the jet elongates, its kinetic energy dissipates, culminating in cavitation at the tip. This induces repeated impacts on the gel fiber surface, forming precise ratchet-like notches.

All fiber types were continuously prepared and collected via a roller system (Supplementary Fig. S18 and Supplementary Movie S1). A ternary phase diagram was established to categorize five morphological types parametrized by spinning solution concentration (C), gas pressure (Pr), and advancement speed of spinning solution (V) (Fig. 3J): cylindrical (1), cavity spindle (2), solid spindle (3), concave ratchet teeth (4), and hybrid spindle fibers (5). Modulating SA concentration and advancement speed not only adjusted hollow spindle spacing but also induced tooth-to-spindle structural transitions (Fig. 3I and Supplementary Fig. S19A–C). 50% drawing ratio results in cavity fibers that resemble bamboo knots instead of spindles (Supplementary Fig. S20). In addition, real-time adjustment of bubble key parameters and

Fig. 3 | Gas−liquid two-phase flow for fibers fabrication. A_{1-4} Bubble flow pattern in the needle. The respective bubble flow pattern formed **B_{1-4}** microscopic images of the gel fibers and **C_{1-4}** microscopic images of the dehydrated fibers, along with **D_{1-4}** SEM images (Q_g = 4.40, 5.35, 6.83 cm³/s, Q_l = 0.05 cm³/s, C = 25 mg/mL and collection rate of 15 rpm). CFD simulations at Q_g/Q_l ratios of **E** 80 (single bubble, Q_g = 4.0 cm³/s Q_l = 0.05 cm³/s, C = 25 mg/mL), **F** 110 (slug bubble, Q_g = 5.5 cm³/s Q_l = 0.05 cm³/s, C = 25 mg/mL) and **G** 140 (annular jet, Q_g = 7.0 cm³/s Q_l = 0.05 cm³/s, C = 25 mg/mL) reveal the interface deformation and flow field dynamics of the two-phase flow. **H** Optical images further capture the critical

stages of gel fiber detachment from the needle tip, illustrating single bubble, slug flow, and annular jet interactions with the gel fibers. **I** Schematic of the bubble-triggered structural transitions in gel fibers. **J** Ternary phase diagram showing fiber morphology regions formed by controlling gas pressure (*Pr*), spinning drop concentration (*C*), and syringe advance speed (*V*). Bubble signal curves detected by the photoelectric sensor under different Q_g/Q_l conditions and the corresponding changes in **K** cavity spindle spacing (L_1), **L** solid spindle spacing (L_2), and **M** tooth spacing (L_3). Scale bar: **B**, **C**: 0.5 mm; **D**: 300 μm; **E**−**H**, and **K**−**M**: 500 μm.
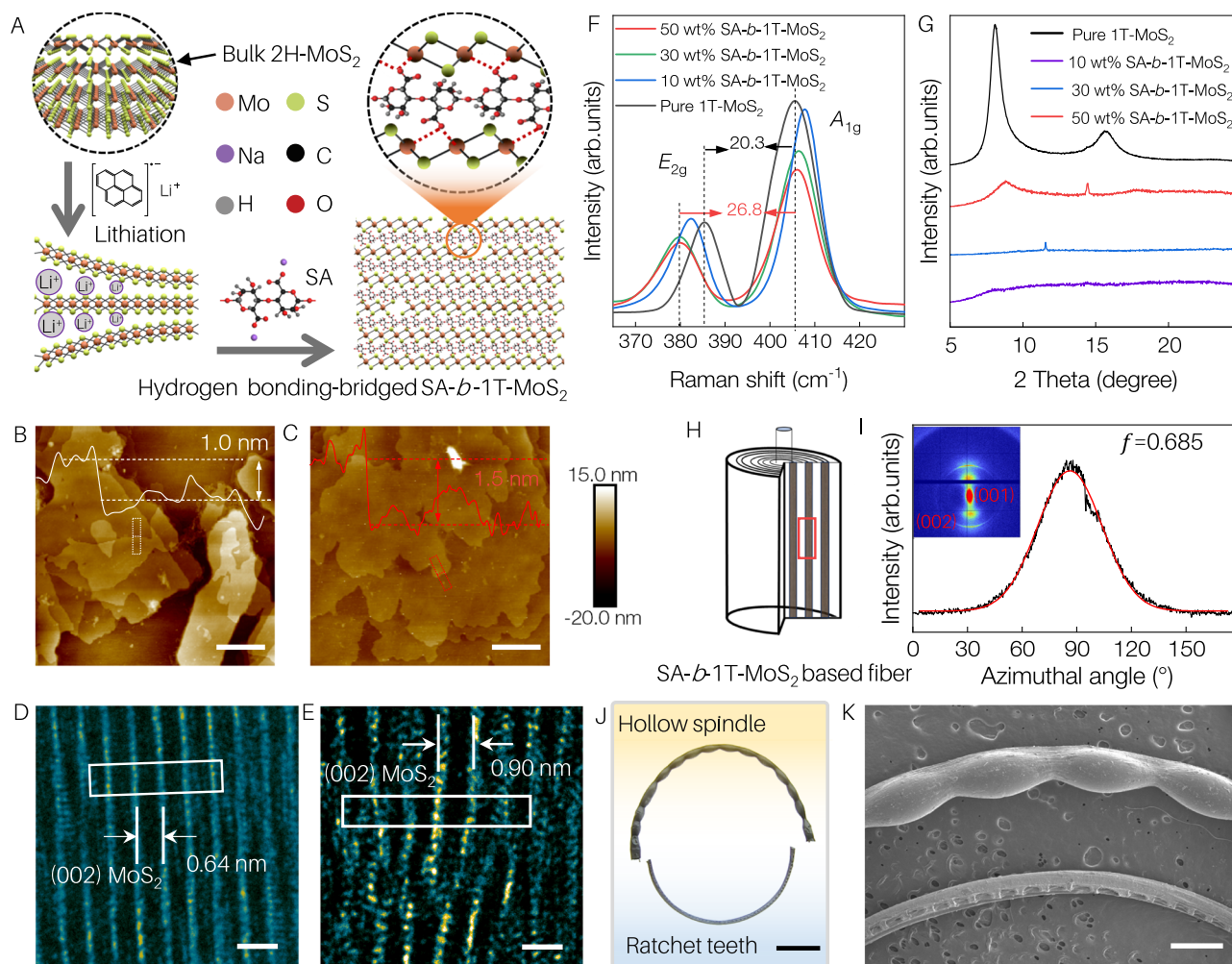
Fig. 4 | Characterization of spinning liquid and fabrication of hydrovoltaic fibers. A Schematic of SA-bridged 1T-MoS$_2$ composite. AFM images **B** before and **C** after SA bridging, the insets showing the thickness profile of a monolayer sheet. TEM images showing the interlayer spacing of 1T-MoS$_2$ sheets **D** before and **E** after SA bridging. Raman spectra **F** and XRD patterns **G** of SA-b-1T-MoS$_2$ with different proportions of 1T-MoS$_2$. **H** Schematic diagram of the ideal fiber crystallization. **I** 2D WAXS scattering pattern and azimuthal scanning profile of the (002) peak of SA-b-1T-MoS$_2$ fiber. The red curve represents the result after fitting. **J** Photographs of representative SA-b-1T-MoS$_2$ cavity spindle knot and concavity ratchet teeth fibers, and **K** corresponding SEM images. Scale bars: **B, C**: 1 µm, **D, E**: 1 nm, **J**: 3 mm, **K**: 900 µm.

morphological changes using the optoelectronic test system enabled precise regulation of the spacing between as-spun fiber units and accurate control of fiber geometries (Fig. 3K–M). Mechanical characterization revealed cavity spindle fibers exhibited high elongation at break, whereas solid spindle and ratchet teeth fibers showed 15–22% lower tensile strength than cylindrical fibers due to structural heterogeneity (Supplementary Fig. S19D). Scalable fabrication yielded diameter ranges of 150–1200 µm (cavity), 300–1000 µm (solid spindle), and 150–1100 µm (ratchet teeth) using standard pipette tips (Supplementary Fig. S21).

Characterization of spinning liquid and fabrication of hydrovolcanic fibers

In our previous work[14,15,46,47], we extensively discussed the tremendous potential of 2D TMDCs in the field of hydrovoltaic. Herein, few-layer 1T-phase MoS$_2$ nanosheets were prepared using an advanced and safe pyrene-lithium compound intercalation method (Supplementary Figs. S22 and S23A–E). SA demonstrated highly spinnable spinning solutions by sequentially MoS$_2$ nanosheets bridging via hydrogen bonding (Fig. 4A). Atomic force microscopy (AFM) results reveal that pristine 1T-MoS$_2$ exhibits a clean and smooth surface with sharp edges, and a top layer step height of approximately 1 nm (Fig. 4B). In contrast,

the surface of SA-bridged 1T-MoS$_2$ (SA-b-1T-MoS$_2$) is covered by other substances, with a top layer step height of 1.5 nm (Fig. 4C). These findings align with the TEM observations (Supplementary Fig. S23E–G). Laser ion beam cutting combined with TEM unraveled that the interlayer spacing increased from approximately 0.65 nm to 0.90 nm before and after bridging (Fig. 4D, E and Supplementary Fig. S24). As shown in Fig. 4F, Raman spectra revealed that with the increase in SA content, the two characteristic peaks of 1T-MoS$_2$ at 385.3 cm^{-1} (E_{2g}) and 405.6 cm^{-1} (A_{1g}) exhibited a blue shift and a red shift, respectively. The increase in the peak interval from 20.03 cm^{-1} to 26.8 cm^{-1} confirmed the change in interlayer spacing. Further analysis of X-ray diffraction (XRD) patterns (Fig. 4G) determined the interlayer spacing changes of SA-b-1T-MoS$_2$. After SA bridging, the (002) diffraction peak at 15.6° weakened and shifted to a lower angle at 11.5°, indicating an expansion of the spacing along the (002) direction by 33.7%. This expansion of interlayer distance is similar to the reports of layered MoS$_2$ compounds in the literature, suggesting that SA has successfully intercalated between the layers of MoS$_2$. At high concentrations (50 wt%), SA-b-1T-MoS$_2$ dispersions formed viscous inks without the aggregation and phase separation of solid particles and dispersion media (Supplementary Fig. S25A). The fluid stretching action aligned the layered materials along the fiber axis, resulting in numerous ordered

crystalline domains in the material (Fig. 4H). The complexation of Ca^{2+} in the coagulation bath further stabilized the interlayer bridging structure of SA-*b*-1T-MoS$_2$ (Supplementary Fig. S25B). According to the 2D small-angle/wide-angle X-ray scattering (SAXS/WAXS) patterns (Fig. 4I), the *Herman* orientation factor (*f*) calculated from the azimuthal scan of the (002) peak indicated that the *f* of SA-*b*-1T-MoS$_2$ fibers was 0.69 (Fig. 4I inset and Supplementary Fig. S26)[48]. This suggests that most of the SA-*b*-1T-MoS$_2$ layers are aligned along the axial direction, and the cross-sectional morphology of the fibers also supports this (Supplementary Fig. S25C). Cavity spindle and concavity ratchet teeth fibers were fabricated by applying SA-b-1T-MoS$_2$ as the spinning solution (Fig. 4J, K).

Fiber-water interaction and hydrovoltaic performances

As shown in Supplementary Fig. S27A, cavity spindle knot fibers exhibited the highest moisture regain, while concavity ratchet teeth fibers showed the fastest rate of change in moisture regain. Compared with solid spindle fibers, water is absorbed by the cavity spindle for 3 s. (Supplementary Fig. S27B and Supplementary Movie S2). Under nitrogen purging at 79% RH, the thermal images show that the cavity spindle fiber absorbs moisture faster and retains it for over 1 min after removal from the high-humidity environment (Fig. 5A, Supplementary Movie S3). This is attributed to their ability to easily absorb water vapor and store it internally (Fig. 5B). At 25.8%, 58.4%, and 95% RH, their water absorption capacities are 47, 121, and 414%, respectively (Fig. 5C). Compared to previously reported hygroscopic materials, these fibers outperform some salt-based materials by over 30% at 90% RH (Supplementary Fig. S27C), demonstrating superior water storage capacity. The optical image (Supplementary Fig. S28A) shows the dynamic water collection process in the spindle structure, where condensation mist forms into small droplets of water and merges toward the center of the knot. This behavior is governed by differences in surface energy and *Laplace* pressure at the knots and junctions (Supplementary Fig. S28B), the water droplets continuously condensed and grew larger, moving towards the fiber knots to form larger droplets. Solid spindle fibers with a diameter of 118 μm were manufactured for mist collection (Supplementary Fig. S28C). Water droplets were collected at the spindle nodes after 150 s in a 0.2 mL/min mist (Supplementary Fig. S28D, E). The water amount increases linearly with time, with only four sharp increases, indicating the migration and coalescence of droplets at the knot (Supplementary Fig. S28F). Compared to the literatures[31,32,49–53], solid spindle fiber exhibited superior fog collection properties (droplet volume per knot diameter) with suitable major axis of knot (Supplementary Fig. S28G). Interestingly, the ratchet fibers collected water from the mist at 0.15 μL/s for 10 s, the grooves were filled with water and transported within 60 s (Fig. 5D, Supplementary Fig. S29A, B and Supplementary Movie S4). This behavior mimics the water transport capabilities of ratchet structures found in plants like *Nepenthes mirabilis* and *Crassula muscosa*[25,54]. Infrared images show that the droplets move directionally to the left (Supplementary Fig. S29C). Microscopic observations revealed that a 2 μL droplet moved against the serrated teeth at a speed of 6890 μm/s (Fig. 5E, Supplementary Movie S5). This is due to the difference in apparent contact angles (θ_1 and θ_2) before and after the groove, which generates a net force (ΔF) along the direction of droplet movement (Fig. 5F, Supplementary Fig. S29D). Figure 5G shows the change in transport distance over time, the speed is initially high and then gradually stabilizes. Our method outperformed spider silk, spines, and smooth surfaces in terms of water collection and transport speed (Supplementary Fig. S29E).

The spinning solution was scalable to polyvinyl alcohol and sodium hydroxyethyl cellulose, demonstrating the versatility and scalability of the method (Supplementary Fig. S30). By uniformly winding carbon nanotube (CNT) fibers on the surface of the prepared fibers, e-fibers were assembled to further explore the applications of these microstructures in flexible electronics (Supplementary Fig. S31A). Among various compositions, the SA-b-1T-MoS$_2$ fibers containing 30 wt% 1T-MoS$_2$ exhibited the broadest response range (11.3% to 82.4% RH) when tested using the device shown in Supplementary Fig. S31B–H. Swapping the electrodes confirmed that the CNT fiber is the positive electrode, and the core layer Mo wire is the negative electrode (Supplementary Fig. S31I). The voltages generated at 85% RH by the traditional cylindrical, cavity spindle, solid spindle, and toothed e-fibers were 0.09, 0.40, 0.11, and 0.15 V, respectively. Their power generation durations were 4, 43, 6, and 4 hours, with sensitivities are 1.93, 0.12, 1.16, and 9.36 mV/RH%/s (Fig. 5H, detailed results in Supplementary Fig. S32). The hydrovoltaic performance differences can be attributed to the distinct water absorption behaviors of the fiber morphologies. Hollow spindle fibers demonstrate superior moisture sorption capacity and sustained kinetics over time, driven by the closed microstructural design. Ratcheted fibers exhibit enhanced initial sorption rates but limited long-term performance, while solid spindle fibers display hygroscopic properties comparable to cylindrical fibers (Fig. 5I, J and Supplementary Fig. S33). The cavity spindle knot e-fibers maintained an open-circuit voltage of 0.4 V for over 43 hours, and the short-circuit current remained above 2.5 μA for more than 33 hours at room temperature (Supplementary Fig. S34). The observed decrease in current was associated with a diminishing external humidity gradient. The e-fibers achieved a power density of 2.18 mW/cm^3 at 0.4 V, lasting 43 h, with an energy conversion efficiency estimated at 15.6%, surpassing most reported humidity-generating fibers (Supplementary Fig. S35A and Table S2). The 5.8 mV/RH% sensitivity and 0.66 s response time of the ratchet e-fiber compare advantageously with numerous literature results (Supplementary Fig. S35B, C and Table S3).

Hydrovoltaic power generation mechanisms

Considering that the SA in the SA-b-1T-MoS$_2$ interlayer contains a large number of hydroxyl (-OH) and carboxyl (-COOH) groups, that could act as proton donors and acceptors, a possible proton transport mechanism under low humidity conditions is provided through proton hopping via hydrogen bonds between carboxyl groups (Supplementary Fig. S36A left). The typical proton hopping conduction follows the equation:

$$\sigma = \sigma_0 \exp\left(-\frac{E_A}{kT}\right) \qquad (2)$$

where σ_0 is the pre-exponential factor, k is the Boltzmann constant, T is the Kelvin temperature and E_A is the activation energy. According to this equation, the proton conductivity of the hopping mechanism is expected to increase with temperature, which is consistent with experimental results obtained by heating the e-fiber under dry conditions (Supplementary Fig. S36B). Since the activation energy for the Grotthuss proton transport mechanism ($E_A = 0.11$ eV) is much lower than that for the proton hopping mechanism ($E_A = 0.5$–0.9 eV), the Grotthuss mechanism of proton transport is achieved through the formation and cleavage of hydrogen bond (H-bond) chains or water molecule networks under high relative humidity (RH) conditions (Supplementary Fig. S36A right). It is well known that H-bond networks are easily disrupted at high temperatures. Consequently, the current of e-fiber rapidly decreases by an order of magnitude when the temperature reaches a critical point of 46.5 °C (Supplementary Fig. S36C). At 80% RH, the electrochemical impedance spectroscopy data show a semicircle in the high-frequency region, while the low-frequency region (controlled by mass transfer) exhibits an elongated "tail" (Supplementary Fig. S36D). This feature is consistent with the typical Grotthuss mechanism spectrum due to its rate-limiting step. By contrast. The observed shorter "tail" at lower RH (50%) is consistent with the proton hopping transport mechanism[55].
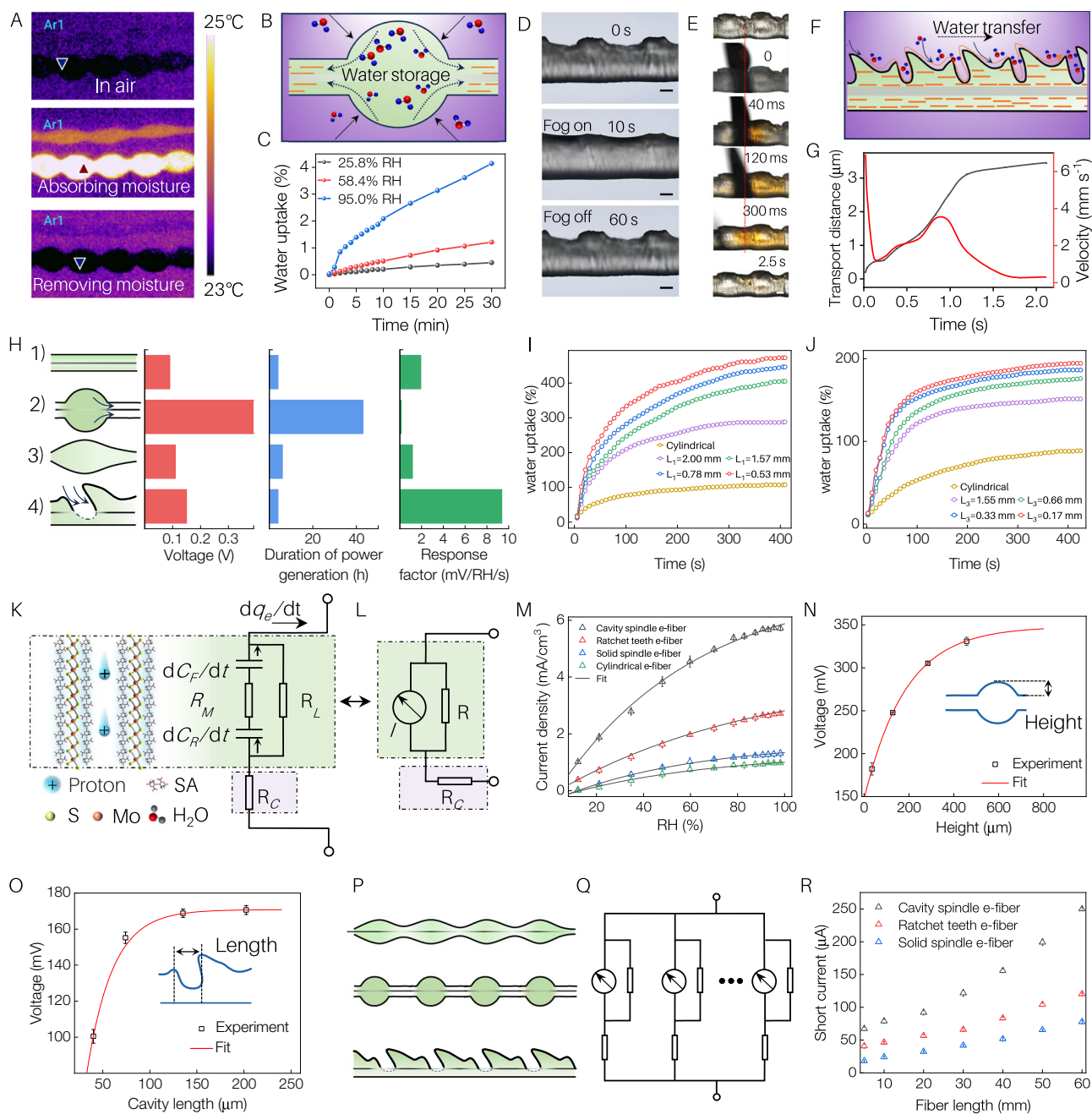
Fig. 5 | Fiber-water interaction and structure-responsive electrical behavior.
A Thermal imaging images of solid spindle and cavity spindle knot fibers.
B Schematic diagram of cavity spindle knot structure for water storage. **C** Water uptake of cavity spindle knot fibers as a function of time at different humidity levels. **D** Optical microscopy images of mist absorption in the grooves. **E** Optical microscope image of the water droplet transfer process between neighboring teeth. **F** Diagram of water transport in ratchet fibers. **G** Plot of the water transport distance as a function of time. **H** Comparison of open-circuit voltage, continuous power generation duration, and response factor for (1) traditional cylindrical e-fibers, (2) cavity spindle e-fibers, (3) solid spindle e-fibers, and (4) toothed e-fibers. Modulation of the unit distance (L) of the microstructure of shaped fibers changes

in their water uptake in **I** hollow spindle fibers and **J** toothed fibers. **K** Equivalent circuit diagram illustrating the structure-responsive hydroelectric based on proton transfer. **L** Corresponding simplified circuit model in **K**. **M** Variation of short-circuit current as a function of humidity for different structures of e-fibers in **H**. ($n = 3$ independent samples, mean ± SD). **N** Voltage variation induced by height changes in cavity spindle fibers. ($n = 3$ independent samples, mean ± SD). **O** Voltage response curve of cavity-toothed e-fibers as a function of cavity length. ($n = 3$ independent samples, mean ± SD). **P, Q** Equivalent parallel circuit configurations for cavity spindles, solid spindles, and toothed fibers at increasing lengths and **R** the respective current increases with length. ($n = 3$ independent samples, mean ± SD). Scale bars: 100 μm.

An in-situ monitoring of the characteristic groups from SA-b-1T-MoS$_2$ using variable-temperature infrared spectroscopy during 20–75 °C is carried out to deepen the understanding of the proton conduction process. The intensity of the O-H stretching region decreases significantly, which may be caused by the evaporation of water (Supplementary Fig. S37A). At the same time, the changes in the C-H stretching region are small, indicating that interactions related to

the hydrophobic C-H groups can be ignored. As shown in Supplementary Fig. S36E, the shift of $v_{as}(COO^-)$ to higher wavenumbers indicates the weakening of hydrogen bonds, while the shift of $v(C-O)$ to lower wavenumbers suggests that C-OH acts as a hydrogen donor and participates in the hydrogen bond structure[56,57]. The possible hydrogen bonding structures, O (3) H···O (5) and O (2) H···O = C-O−, were deduced from the *Noda's* rule of judging and the simplified

method proposed by Wu et al. (Supplementary Figs. S36F, G and S37B)[58] and from the structure of SA[59,60] (Details are described in the Supplementary Table S4 and Table S5). Supplementary Fig. S36H shows the molecular structure under the Grotthuss mechanism with water molecules participating in building hydrogen bond networks in the wet state, and the intramolecular hydrogen bonds involved in proton hopping in the dry state.

Mechanism of structure-responsive hydrovoltaics

The underlying mechanisms driving the distinct hydrovoltaic performance across fiber architectures were investigated. Heterostructured fibers enable interlayer proton transfer via spontaneous moisture absorption, generating an electric potential. This dynamic moisture absorption-release cycle mirrors capacitor charging (C_F) and discharging (C_R) processes. The equivalent circuit is shown in Fig. 5K, L, where R_L, R_M, and R_C, represent the resistances of water, SA-1T-MoS$_2$ composites, and contact resistance with the outer electrode, respectively. The equivalent current is derived as $I = \frac{dq_e}{dt} = -\varphi S C_0 \upsilon_0 (1 - e^{-\alpha H})(0.05 \leq \alpha \leq 8.3)$, where φ is defined as the equivalent surface potential of SA-1T-MoS$_2$ relative to the adsorbed water layer, S is the fiber cross-sectional area, C_O is the material-specific pseudocapacitance, υ_0 represents the maximum velocity of water movement at high humidity, α is the fiber structure-dependent parameter. Current density increases with RH but saturates near 100% RH, consistent with the proposed model (Fig. 5M). The enlarged cavity dimensions in hollow spindle and ratchet fibers amplify axial humidity gradients, accelerate water migration kinetics, and elevate output voltages (Fig. 5N, O). This structural modulation aligns with the equivalent circuit model, where increased fiber length corresponds to parallel resistor configurations, driving a linear rise in current with length (Fig. 5P–R). These experimental observations validate the proposed mechanistic framework and circuit analogy.

Hydrovoltaic applications of fibers

Interestingly, the excellent response of e-fiber sensors to weak signals makes them very suitable for monitoring slight disturbances in the environment, such as tiny water droplets, mist, and non-contact finger changes (Fig. 6A–C). A bionic power-generating spider web made from cavity spindle knot e-fiber generated electricity of 1.2 V for 25 hours continuously, sufficient to run a calculator (Fig. 6D–F and Supplementary Movie S6). Ratchet e-fiber shows potential in human-machine interface applications. The e-fiber could be easily integrated as a respiratory sensor into commercially available masks or sewn into fabrics to create interactive masks (Fig. 6G). An N95 mask was equipped with e-fiber sensors to monitor respiratory activities, such as normal breathing, post-exercise breathing, and obstructive sleep apnea-hypopnea syndrome (Fig. 6H and Supplementary Fig. S38). To illustrate the advantages of e-fiber in respiratory sensing, a mask that can accommodate the e-fiber and fit the face was created (Fig. 6I left and Supplementary Fig. S39A–D). An integrated respiratory monitoring diagnostic, and treatment system was designed and demonstrated for its application. The system consists of a signal collection unit (e-fiber), a signal processing unit (Arduino), a signal transmission unit (wireless connection module), a control unit (Arduino), an output unit (LED), and a buzzer (Supplementary Figs. S39E–H and S40). This system collects respiratory data and uploads it in real-time via a wireless network to a terminal such as a phone or computer (Fig. 6J and Supplementary Movie S7), enabling telemedicine applications. It is accepted that changes in the nasal cycle can serve as diagnostic indicators for professionals (Fig. 6K). The special design of the mask separates left and right nasal airflow and correctly guides it to the response chamber (Fig. 6L). The smart mask is highly flexible, easy to wear, and conforms to the face. (Fig. 6M, N). The e-fibers are fixed in the multi-cavity chamber of the mask for easy replacement (Fig. 6O). Smart mask and as a proof of concept, we exhibit round-the-clock monitoring of nasal breath with a smart mask (Fig. 6P, Q and

Supplementary Fig. S41). The overall trend of the two nasal breathing curves can be used to statistically analyze the nasal cycle (Fig. 6R, S).

Discussion

In summary, we have developed a gas–liquid two-phase flow spinning system capable of rapidly fabricating diverse high-performance shaped fibers. By leveraging bubble-driven flow regimes (single, slug, and annular), this method enables programmable fiber morphogenesis through controlled gas–liquid flow rates without spinneret modification. Systematic mapping of bubble formation zones in aqueous and SA solutions revealed distinct pattern transitions, validated through computational fluid dynamics simulations and mechanistic modeling of bubble-triggered gel transformations. The platform's versatility is demonstrated through extension to alternative spinnable polymers (e.g., polyvinyl alcohol, hydroxyethyl cellulose sodium) and composite systems like SA-interlayer-bridged MoS$_2$. Resultant fibers exhibit enhanced functionalities, including moisture sorption (cavity spindle fibers of 414% water uptake at 95% RH), mist collection (solid spindle fibers achieve a fog collection capacity of 44.6 μL/mm), and directional water transport of 6890 μm/s.

Fundamental investigations into the interlayer architecture of SA-b-1T-MoS$_2$, alongside the mechanistic transition between proton-hopping and Grotthuss proton conduction, establish a scalable platform for functional fiber applications in energy technologies. This structural precision underpins our proposed structure-responsive hydrovoltaic theory, where fiber architectures govern humidity gradient dynamics. The electrical response and recovery time of the cavity spindle knot e-fibers exceeds 100 s, producing a power density of 2.18 mW/cm^3, 15.6% energy conversion efficiency, stable voltage of 0.40 V in the air, and generating electricity stably for more than 43 h. The developed cavity spindle knot fibers bionic spiderweb generates electricity continuously for more than 1.2 V, which is sufficient for running a calculator. The electrical response and recovery time of the concavity ratchet teeth fibers are only 0.66 s, sensitivity is 5.8 mV/RH%. Integrated into smart respiratory masks for real-time apnea detection and rhythm monitoring, enabling transformative telehealth applications. This strategy bridges advanced fiber engineering with sustainable technologies, offering a universal framework for structure-function integrated design. By correlating fiber morphologies with hydrovoltaic optimization, we enable multimodal applications in energy, environmental sensing, and biomedicine.

Methods

Materials

SA (viscosity: 200 ± 20 mPa.s), commercial molybdenum disulfide (MoS$_2$, 98%) from Shanghai Aladdin Chemical Reagent Co., Ltd. Pyrene (Py, ≥98%), 1,2-Dimethoxyethane (DME, 99%, water≤50ppm (by K.F.), Safe Dry) were purchased from Adamas-beta. Li metal were obtained from HF-Kejing Materials Technology Co., Ltd. The hydrolyzed commercial PVA (Dongyang Syn Co.) molecular weight of 17,000, sodium carboxymethyl cellulose (250 kDa, the degree of substitution for the used CMC was 0.8, medium viscosity), aluminum sulfate octadecahydrate (Al$_2$(SO$_4$)$_3$·18H$_2$O) was purchased from Sigma-Aldrich (Milwaukee). Spinning nozzle (24 gauge–13 gauge–30 gauge (corresponding to the inner, outer diameters, and gas phase of 250, 1900, and 120 μm, respectively) purchased from Hefei Sipin Technology Co. ltd. Molybdenum wire (diameter: 80 μm) purchased from Nanjing Aoshuo Metal & Plastic Co., Ltd. CNT fiber (Diameter: 60–80 μm, Elongation at break: 15–25%) were obtained from Nanjing XianFeng Nano Material Technology Co., Ltd.

A PES-based gas–liquid mixing pipeline technique for the detection of two-phase flow patterns

The commercial photodetector (Shengtai Technology Co., Ltd.) is clamped to a horizontally placed target pipe (2 mm diameter)
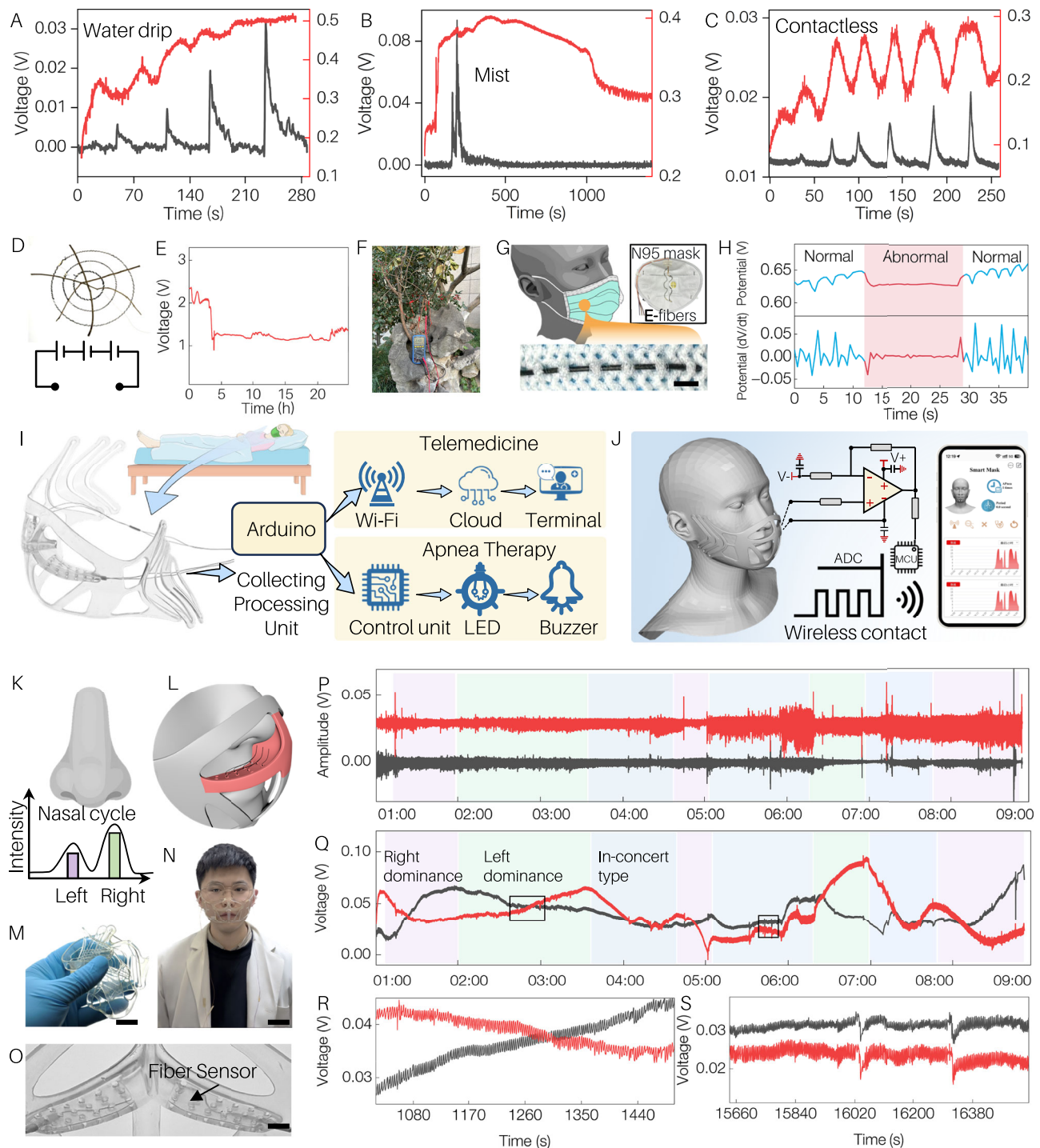
Fig. 6 | Hydrovoltaic applications of fibers. The output characteristics of concavity ratchet teeth fibers (black curve) and cavity spindle knot fibers (red curve) e-fibers in response to **A** droplet, **B** mist impact, and **C** finger contactless. **D** Cavity spindle knot fibers were wound on three Mo rings (diameter: 20, 12, and 5 cm) and then the electrodes were fabricated in series to obtain a bionic spider web to power generation. **E** Continuous power generation capacity of the bionic spider web. **F** The electricity generated by the bionic spider web could operate a calculator. Donghua University (121°24′E 31°12′N); date: Jan. 25, 2024; temperature: 0–6 °C; humidity: 54%; wind speed:11 km/h. **G**, **H** Schematic illustration of the application of e-fibers, which could be easily integrated into the inner lining of a regular mask to monitor human respiration and could be simply sewn into fabrics. **I** Schematic of an integrated respiration monitoring-therapy-telemedicine system based on e-fibers. **J** The system is composed of a smart mask, charge collection circuit, microprocessor, and wireless transmission circuit. **K** Illustration of the human nasal cycle. **L** Illustration of nasal airflow guidance in a smart mask. **M** Flexible demonstration of the smart mask. **N** Photograph of a subject wearing the monitoring system. **O** Diagram showing the installation of e-fibers in the smart mask. **P** Amplitude graph of dual-channel sleep respiration signals collected from the subject (male, 28 years old) over one night. Red curve: right breath, black: left breath. **Q** Raw signal voltage graph and corresponding locally enlarged views (R and S) of the sleep respiration signals. Scale bars, **G**: 2 mm, **M**: 1 cm, **N**: 5 cm, **O**: 6 mm.

with the end of the pipe connected to a custom-designed biaxial spinning nozzle with the size of 24 gauge-13 gauge. The center needle is vented into the air stream. The outer layer is fed with liquid. The photodetector is supplied with a 5 V power supply, and the analog signal output is connected to a Keithley 6514 for signal acquisition.

Synthesis of sequentially bridged MoS_2 sheets

SA solution (5 mg/mL) was mixed with freshly prepared 1T-MoS_2 powder by stirring for 30 minutes, and then ultrasonicated (60 W) for 2 minutes in an ice bath. The resulting homogeneous dispersion was then stirred for 24 hours to form a freestanding hydrogen-bonding-bridged 1T-MoS_2 sheet. To test the phase of the bridged SA-b-1T-MoS_2, the reaction mixture was stirred at 40 °C for 24 hours using a centrifugation washing method and repeatedly washed with deionized water for 6 days to remove free SA particles, resulting in a clean SA-b-1T-MoS_2 dispersion, which was then freeze-dried. Based on the amount of 1T-MoS_2 added, the following three hydrogens bonding-bridged 1T-MoS_2 sheets were prepared: SA-b-1T-MoS_2-I (10 wt%), SA-b-1T-MoS_2-II (30 wt%), and SA-b-1T-MoS_2-III (50 wt%). Additionally, based on the concentration of the SA solution, the following four kinds of SA-b-1T-MoS_2 spinning solutions were prepared: SA-b-1T-MoS_2-I (5 mg/mL), SA-b-1T-MoS_2-II (10 mg/mL), SA-b-1T-MoS_2-III (20 mg/mL), SA-b-1T-MoS_2-IV (30 mg/mL), and SA-b-1T-MoS_2-V (50 mg/mL).

Spinning fibers with gas–liquid two-phase flow spinning method

All the spinning solutions were defoamed with a degassing machine before use and then injected via a custom-designed biaxial spinning nozzle with a size of 24 gauge−13 gauge (corresponding to the inner diameter of 250 μm and outer diameter of 1900 μm). As shown in Supplementary Fig. S5, in a wet-spinning-based device, we employed a gas nozzle (120 μm) as the gas-phase input, which was located 2 cm from the outlet of the spinning solution, using nitrogen as the dispersed phase. A lab-made propulsion pump and a precision pressure controller (Marsh BELLOFRAM, T70, USA, equipped with a digital display, KITA SENSOR, KP43C, Taiwan) were used to inject the spinning solution and nitrogen gas, respectively. The pipeline was equipped with a check valve (SMC, Japan). The resultant gas–liquid mixture flow was collected in a 5 wt% $CaCl_2$ solution to form solidified multifaceted fibers. A rotating collection roller collected solidified fibers from the $CaCl_2$ solution. The diverse morphology fibers were directly and manually spun from the wet-spinning gel under bubble-triggered spinning liquid deformation conditions. For instance, by adjusting the gas pressure (0 kPa-16 kPa), the gas–liquid two-phase flow in the pipeline could spontaneously form hollow spindle-shaped fibers, solid spindle fibers, and rachet tooth fibers from single continuous bubbles, slug bubbles, and annular jets. Alternatively, adjusting the viscosity of the spinning solution and the propulsion speed could also control the formation of different morphologies of fibers. Additionally, the drawing speed could be adjusted to achieve a specific distance between adjacent units. Finally, the extruded fibers were soaked in a water bath for a few minutes and then lifted out to dry naturally overnight.

Fabrication of hydrovoltaic fibers

The SA-b-1T-MoS_2/metal fibers and CNT fibers are core-shell fibers. The shell fibers (CNT) were twined around the core fibers (the four types of fibers). Two identical motors were placed opposite each other, and the ends of the respective fibers were fixed on the motors. Then, the movement of the nanotube fibers along the fiber axis is driven by a linear stage. One end of the CNT fiber was fixed to the core fiber, and as the pair of synchronously running motors and sliders operated, the CNT was uniformly wound around the surface of the core fiber. Finally, hydrovoltaic fibers were obtained, with the core molybdenum wire serving as the cathode and the outer layer of CNT fibers serving as the anode.

Performance test of the hyrdrovoltaic

The electrical measurement was recorded in real-time using a Keithley 6514 electrometer controlled by a LabView-based data acquisition system. Ambient temperature and humidity are controlled with a chamber. The environmental temperature and humidity were monitored by using a hygrometer (GSP-8, Jiangsu Jingchuang Electronics Co., Ltd). The humidity environments were achieved using saturated aqueous solutions of pure N_2, LiCl, $CaCl_2 \cdot 6H_2O$, $MgNO_3$, NaCl, and K_2SO_4 in a closed glass vessel at an ambient temperature of ~25 °C, which yielded approximately 0%, 11.3%, 16.7%, 25.8%, 45.4%, 58.4%, 77.3%, and 82.4% RH, respectively. The flow rate for the response speed test was about 300 sccm. The hydrovoltaic fiber reacts with moisture in a test chamber equipped with electrode probes, temperature and humidity sensors (GSP-8, Jiangsu Jingchuang Electronics Co., Ltd, China), and a heating unit (IST 600E, Beijing Sinoagg Co., Ltd, China). The fibers tested had a radius of 500 μm and a length of 5 cm. Unless specified otherwise, the experiments were conducted at 25 °C and 1 atm. For the temperature stability test, the temperature ranged from 0 to 60 °C. Each test was performed independently three times, yielding consistent results. Data were analyzed through Origin 2021 edu.

Fabrication of a spider web for hydrovoltaic generation

Molybdenum wires were woven into a spider web model, featuring three concentric circles with diameters of 20 cm, 12 cm, and 5 cm, from the outermost to the innermost circle. CSK e-fibers were uniformly wrapped around the molybdenum wires. This setup formed a typical symmetric electrode water photovoltaic generator, where the inner and outer molybdenum wires served as the anode and cathode, respectively, consistent with the operating mechanism. By connecting three such units in series, a spider web humidity generator was created.

3D printing of smart masks

Using a digital light processing printer (405 nm 2000 mW, Lite600HD, Zhejiang Zhechuang 3D Technologies Co., Ltd., China). Polyurethane-resin ink (WeNext Technology Co., Ltd., China) was fabricated. The spot diameter ranged from 0.12 to 0.20 mm, the layer thickness was 50–250 μm, and the light intensity was 11.37 mW cm^{-2}. Finally, the object was cleaned with TDW. The STL files were programmed in DeScribe (Nanoscribe GmbH), with a height distance of 8 cm and a laser power of 100%. Lastly, the CRT e-fibers were placed in the uniquely designed positions of the printed mask.

The small- and wide-angle X-ray scattering

The SAXS and WAXS data of the fibers were obtained by utilizing a Xeuss 3.0 (Xenocs, France). The light tube power was 30 W (wavelength 1.54 Å). Analysis was carried out using an Eiger2R 1 M detector, and the sample-detector distance was set to ~80 mm. The 2D scattering pattern is obtained from FIT2D v2.4.2.0. The authors extend their gratitude to Mr. Shuchun Wang from Scientific Compass (www.shiyanjia.com) for providing invaluable assistance with the SAXS analysis.

Temperature-variable FTIR measurement

500 μL of SA-b-1T-MoS_2 precursor was drop-cast onto a CaF_2 window sheet, and the excess water was naturally evaporated to obtain a thin film, which was then incubated in a chamber at 80% RH for 12 hours. The film was then incubated in a chamber at 80% RH for 12 hours. It was finally encapsulated with another CaF_2 sheet. For temperature-controlled measurements, the sealed samples were heated from 20 °C to 75 °C at 5 °C intervals on a Nicolet iS50 FTIR spectrometer in transmission mode.

Two-dimensional correlation spectroscopy

Temperature-dependent FTIR spectra of SA-*b*-1T-MoS$_2$, recorded from 20 to 75 °C, were utilized for two-dimensional correlation analysis. The 2D correlation analysis was performed using 2D Shige ver. 1.3 software (© Shigeaki Morita, Kwansei-Gakuin University, Japan, 2004–2005), and the resulting data were visualized as contour plots using Origin (Origin 2021 edu). In these contour plots, warm colors (red and yellow) indicate positive intensities, while cool colors (blue) represent negative intensities.

Demonstration of smart mask on respiratory monitoring

An electronic fiber sensor was integrated into the mask. Respiratory data were gathered by Arduino, which also processed and evaluated the data in real-time. Based on the analysis, Arduino controlled an LED and buzzer. It is worth noting that an important method for treating apnea is timely intervention when apnea occurs, such as waking the patient to resume active breathing. The smart mask diagnostic system detects apnea, the LED emits a red light, and the buzzer alerts to prevent further danger. Only one volunteer, aged 28 years, male, participated in respiratory data collection and signed informed consent prior to this experiment. We confirm that consent to publish identifiable images was obtained from all participants involved, in accordance with the conditions set out in the Nature Portfolio participant release form. Consent was obtained for the publication of images identifying the study subject.

General characterization

The morphology and composition of as-prepared samples were investigated by scanning electron microscopy (SEM S3400), provided with energy dispersive X-ray spectroscopy and high-resolution transmission electron microscopy (HR-TEM) (Talos 200). The three-dimensional morphology of the fibers was characterized by Micro-CT (IMAGING 100; Raycision Medical Technology Co., Ltd, China). The topography of the MoS$_2$ flake was characterized by AFM (MultiMode 8-HR, Bruker, Germany). Fourier-transform infrared (FTIR) spectra were collected by a Thermo IS 50 spectrometer. XRD patterns were recorded on a D2 PHASER diffractometer with Cu-Kα radiation (Bruker, Germany) at a generator current of 100 mA used as the radiation source, and the generator voltage was set as 30 kV with a scan step size of 0.02°, 2θ rotates 4° min^{-1}. Electrical impedance measurements were performed using an electrochemical workstation PGSTAT302N (Metrohm Autolab). Keithley 6514 was used to measure the voltage drop. High-resolution Raman spectra were performed using a Raman microscope system (LabRAM, Horiba Jobin Yvon, France) with a 514 nm wavelength laser. The sorption kinetics curves were measured in a glove box with a balance measuring the weight of the fibers under constant temperature and humidity.

Demonstration of e-fiber on telemedicine

Two CRT e-fiber sensors were embedded in the mask. Breathing data were collected using Arduino and transmitted to the cloud via the ESP8232 Wi-Fi module. The respiratory data were monitored in real-time on a website (WebSockets) accessible via a smartphone (iPhone 15) or a computer. The cloud data was further analyzed using a Python program and displayed on a laptop (ASUS GU603HR-0005). The authors affirm that human research participants provided informed consent for publication of the images in Fig. 6N.

Statistics and reproducibility

All data are expressed as mean ± standard deviation. In the microscope experiments, three independent experiments were performed, and representative images were shown. The data analysis and display were realized in Origin.

Ethics declarations

This study was approved by Donghua University Science and Technology Ethics Committee (NO. SRSY202410110047). The informed consent of the participant was obtained prior to this experiment.

Source data

https://figshare.com/s/b1fad1bd8a771c8ed0f4.

Reporting summary

Further information on research design is available in the Nature Portfolio Reporting Summary linked to this article.

Data availability

The experimental data generated in this study have been deposited in the Figshare repository under accession code [https://figshare.com/s/b1fad1bd8a771c8ed0f4]. The respiratory detection analysis code generated in this study is available in the GitHub repository (https://github.com/yuanmingcao/Respiratory_detection). Processed data supporting the findings are provided in the Supplementary Information files. Source data for all figures are included with this paper.

Code availability

The source codes for apnea diagnosis, recognition, treatment, and codes for telemedicine and human–machine interaction used in this study are available at https://github.com/yuanmingcao/Respiratory_detection[61].

References

1. Zhang, Z. et al. Emerging hydrovoltaic technology. *Nat. Nanotechnol.* **13**, 1109–1119 (2018).
2. Yin, J., Zhou, J., Fang, S. & Guo, W. Hydrovoltaic energy on the way. *Joule* **4**, 1852–1855 (2020).
3. Shao, B. et al. Electricity generation from phase transitions between liquid and gaseous water. *Adv. Energy Mater.* **13**, 2204091 (2023).
4. Wang, X. et al. Hydrovoltaic technology: from mechanism to applications. *Chem. Soc. Rev.* **51**, 4902–4927 (2022).
5. Sun, Z. et al. Achieving efficient power generation by designing bioinspired and multi-layered interfacial evaporator. *Nat. Commun.* **13**, 5077 (2022).
6. Wang, L., Zhang, W. & Deng, Y. Advances and challenges for hydrovoltaic intelligence. *ACS Nano* **17**, 14229–14252 (2023).
7. Xu, J. et al. Sustainable moisture energy. *Nat. Rev. Mater.* **9**, 722–737 (2024).
8. Xia, H. et al. Electricity generated by upstream proton diffusion in two-dimensional nanochannels. *Nat. Nanotechnol.* **19**, 1316–1322 (2024).
9. Xue, G. et al. Water-evaporation-induced electricity with nanostructured carbon materials. *Nat. Nanotechnol.* **12**, 317–321 (2017).
10. Zhang, Y. et al. An asymmetric hygroscopic structure for moisture-driven hygro-ionic electricity generation and storage. *Adv. Mater.* **34**, 2201228 (2022).
11. Tan, J. et al. Self-sustained electricity generator driven by the compatible integration of ambient moisture adsorption and evaporation. *Nat. Commun.* **13**, 3643 (2022).
12. Li, L. et al. A flexible tough hydrovoltaic coating for wearable sensing electronics. *Adv. Mater.* **35**, 2304099 (2023).
13. Jin, H. et al. Identification of water-infiltration-induced electrical energy generation by ionovoltaic effect in porous CuO nanowire films. *Energy Environ. Sci.* **13**, 3432–3438 (2020).
14. Xue, Y.-B. et al. Asymmetric sandwich Janus structure for high-performance textile-based thermo–hydroelectric generators toward human health monitoring. *Adv. Funct. Mater.* **34**, 2310485 (2024).

15. Cao, Y.-M. et al. Vertical phase-engineering MoS₂ nanosheet-enhanced textiles for efficient moisture-based energy generation. *ACS Nano* **18**, 492–505 (2024).

16. Chen, C. et al. Functional fiber materials to smart fiber devices. *Chem. Rev.* **123**, 613–662 (2023).

17. Guan, Q.-F. et al. Lightweight, tough, and sustainable cellulose nanofiber-derived bulk structural materials with low thermal expansion coefficient. *Sci. Adv.* **6**, eaaz1114 (2020).

18. Sun, Z. et al. Hyperstable eutectic core-spun fiber enabled wearable energy harvesting and personal thermal management fabric. *Adv. Mater.* **36**, 2310102 (2024).

19. Yang, C., Yu, Y., Shang, L. & Zhao, Y. Flexible hemline-shaped microfibers for liquid transport. *Nat. Chem. Eng.* **1**, 87–96 (2024).

20. Shang, L. et al. Spinning and applications of bioinspired fiber systems. *ACS Nano* **13**, 2749–2772 (2019).

21. Chen, H. et al. Continuous directional water transport on the peristome surface of Nepenthes alata. *Nature* **532**, 85–89 (2016).

22. Li, J., Li, J., Sun, J., Feng, S. & Wang, Z. Biological and engineered topological droplet rectifiers. *Adv. Mater.* **31**, 1806501 (2019).

23. Ju, J. et al. A multi-structural and multi-functional integrated fog collection system in cactus. *Nat. Commun.* **3**, 1247 (2012).

24. Zheng, Y. et al. Directional water collection on wetted spider silk. *Nature* **463**, 640–643 (2010).

25. Li, C., Yu, C., Zhou, S., Dong, Z. & Jiang, L. Liquid harvesting and transport on multiscaled curvatures. *Proc. Natl Acad. Sci. USA* **117**, 23436–23442 (2020).

26. Peng, L. et al. Bioinspired artificial spider silk photocatalyst for the high-efficiency capture and inactivation of bacteria aerosols. *Nat. Commun.* **14**, 2412 (2023).

27. Wu, H., Mendel, N., van den Ende, D., Zhou, G. & Mugele, F. Energy harvesting from drops impacting onto charged surfaces. *Phys. Rev. Lett.* **125**, 078301 (2020).

28. van der Heyden, F. H. J., Stein, D. & Dekker, C. Streaming currents in a single nanofluidic channel. *Phys. Rev. Lett.* **95**, 116104 (2005).

29. Yin, J. et al. Generating electricity by moving a droplet of ionic liquid along graphene. *Nat. Nanotechnol.* **9**, 378–383 (2014).

30. Blackledge, T. A. et al. Reconstructing web evolution and spider diversification in the molecular era. *Proc. Natl Acad. Sci. USA* **106**, 5229–5234 (2009).

31. Wang, S. et al. Bioinspired robust helical-groove spindle-knot microfibers for large-scale water collection. *Adv. Funct. Mater.* **33**, 2305244 (2023).

32. Xie, R. et al. Necklace-like microfibers with variable knots and perfusable channels fabricated by an oil-free microfluidic spinning process. *Adv. Mater.* **30**, 1705082 (2018).

33. Tian, X., Chen, Y., Zheng, Y., Bai, H. & Jiang, L. Controlling water capture of bioinspired fibers with hump structures. *Adv. Mater.* **23**, 5486–5491 (2011).

34. Wu, J., Wang, N., Zhao, Y. & Jiang, L. Electrospinning of multilevel structured functional micro-/nanofibers and their applications. *J. Mater. Chem. A* **1**, 7290–7305 (2013).

35. Zhu, P. & Wang, L. *Microfluidics-Enabled Soft Manufacture*. (Springer International Publishing, Cham, 2022).

36. Tian, Y. et al. Large-scale water collection of bioinspired cavity-microfibers. *Nat. Commun.* **8**, 1080 (2017).

37. Shang, L. et al. Bioinspired multifunctional spindle-knotted microfibers from microfluidics. *Small* **13**, 1600286 (2017).

38. Ji, X., Guo, S., Zeng, C., Wang, C. & Zhang, L. Continuous generation of alginate microfibers with spindle-knots by using a simple microfluidic device. *RSC Adv.* **5**, 2517–2522 (2015).

39. Zhang, M. et al. Programmable dynamic interfacial spinning of bioinspired microfibers with volumetric encoding. *Mater. Horiz.* **8**, 1756–1768 (2021).

40. Kota, A. K., Kwon, G. & Tuteja, A. The design and applications of superomniphobic surfaces. *NPG Asia Mater.* **6**, e109–e109 (2014).

41. Mamoru, I. & Takashi, H. Thermo-fluid dynamics of two-phase flow. https://link.springer.com/book/10.1007/978-1-4419-7985-8 (Springer Science & Business Media, 2010).

42. Chen, H. et al. Biomimetic air purification with liquid-gating topological gradient microfluidics. *Nat. Chem. Eng.* **1**, 650–660 (2024).

43. Acerce, M., Voiry, D. & Chhowalla, M. Metallic 1T phase MoS₂ nanosheets as supercapacitor electrode materials. *Nat. Nanotechnol.* **10**, 313–318 (2015).

44. He, D. et al. Electricity generation from phase-engineered flexible MoS₂ nanosheets under moisture. *Nano Energy* **81**, 105630 (2021).

45. Zhao, G. et al. Hydrogel-assisted microfluidic spinning of stretchable fibers via fluidic and interfacial self-adaptations. *Sci. Adv.* **9**, eadj5407 (2023).

46. Han, B.-B. et al. Hydrophilic 1T-WS₂ nanosheet arrays toward conductive textiles for high-efficient and continuous hydroelectric generation and storage. *Small* **20**, 2308527 (2024).

47. Luo, P. et al. Nanosheets array-induced nanofluidic channels toward efficient primary batteries-coordinated textiles. *Nano Energy* **118**, 108988 (2023).

48. Gu, J. et al. Extremely robust and multifunctional nanocomposite fibers for strain-unperturbed textile electronics. *Adv. Mater.* **35**, 2209527 (2023).

49. Song, C., Zhao, L., Zhou, W., Zhang, M. & Zheng, Y. Bioinspired wet-assembly fibers: from nanofragments to microhumps on string in mist. *J. Mater. Chem. A* **2**, 9465–9468 (2014).

50. Bai, H. et al. Direction controlled driving of tiny water drops on bioinspired artificial spider silks. *Adv. Mater.* **22**, 5521–5525 (2010).

51. Liu, H. et al. Highly efficient water harvesting of bioinspired spindle-knotted microfibers with continuous hollow channels. *J. Mater. Chem. A* **10**, 7130–7137 (2022).

52. Shi, R. et al. Hourglass-shaped microfibers. *ACS Appl. Mater. Interfaces* **12**, 29747–29756 (2020).

53. Zou, T. et al. Porous spindle-knot fiber by fiber-microfluidic phase separation for water collection and nanopatterning. *ACS Appl. Mater. Interfaces* **16**, 49823–49833 (2024).

54. Yang, L. et al. Selective directional liquid transport on shoot surfaces of Crassula muscosa. *Science* **384**, 1344–1349 (2024).

55. He, J. et al. High performance humidity fluctuation sensor for wearable devices via a bioinspired atomic-precise tunable graphene-polymer heterogeneous sensing junction. *Chem. Mater.* **30**, 4343–4354 (2018).

56. Bakkas, N., Bouteiller, Y., Loutellier, A., Perchard, J. P. & Racine, S. The water-methanol complexes. Matrix induced structural conversion of the 1-1 species. *Chem. Phys. Lett.* **232**, 90–98 (1995).

57. Watanabe, A., Morita, S. & Ozaki, Y. Study on temperature-dependent changes in hydrogen bonds in cellulose iβ by infrared spectroscopy with perturbation-correlation moving-window two-dimensional correlation spectroscopy. *Biomacromolecules* **7**, 3164–3170 (2006).

58. Sun, S. & Wu, P. Spectral insights into microdynamics of thermo-responsive polymers from the perspective of two-dimensional correlation spectroscopy. *Chin. J. Polym. Sci.* **35**, 700–712 (2017).

59. Chen, K., Shi, B., Yue, Y., Qi, J. & Guo, L. Binary synergy strengthening and toughening of bio-inspired nacre-like graphene oxide/sodium alginate composite paper. *ACS Nano* **9**, 8165–8175 (2015).

60. Çaykara, T., Demirci, S., Eroğlu, M. S. & Güven, O. Poly(ethylene oxide) and its blends with sodium alginate. *Polymer* **46**, 10750–10757 (2005).

61. Cao, Y. et al. Code for gas–liquid two-phase bubble flow spinning for hydrovoltaic flexible electronics. *Zenodo* https://doi.org/10.5281/zenodo.15162011 (2025).

Author contributions

X.L. conceived the idea and supervised the research. X.L. and Y.C. designed the experiments. J.Q. and X.L. designed and constructed the experimental system. H.Z., J.T., T.S., X.Z., and S.G. performed the modeling and simulations. M.Z., Y.D., C.W., P.H., J.T., Y.C., and X.L. synthesized the specimens and performed the analysis of different characterizations. J.T., Y.D., M.Z., M.Z., S.G., Y.C., and X.L. contributed to writing the manuscript.

Competing interests

A patent (CN202410403096.X) for the shaped fiber spinning method has been applied on behalf of Donghua University. X.L. and Y.C. are listed as inventors. The authors declare no other competing interests.

Additional information

Supplementary information The online version contains supplementary material available at https://doi.org/10.1038/s41467-025-59585-6.

Correspondence and requests for materials should be addressed to Jiajun Qiu or Xuanyong Liu.

Peer review information *Nature Communications* thanks Wei Deng, and the other, anonymous, reviewer(s) for their contribution to the peer review of this work. A peer review file is available.

Reprints and permissions information is available at http://www.nature.com/reprints

Publisher's note Springer Nature remains neutral with regard to jurisdictional claims in published maps and institutional affiliations.